Structural lifetime assessment for the DEMO divertor targets: Design-by-analysis approach and outstanding issues

J.H. You*, M. Li[1], K. Zhang

Max Planck Institute for Plasma Physics, Boltzmann Str. 2, 85748 Garching, Germany

Abstract

Divertor targets of a nuclear fusion reactor are exposed to harsh loading environments comprising high heat flux, varying stresses and neutron irradiation. For a robust design, the structural integrity must be assured against complex failure modes for the envisaged operation scenarios in order to ensure the required lifetime. To this end, the lifetime against structural failure needs to be assessed by means of either experimental tests (design-by-experiment) or computational analyses (design-by-analysis). In the latter approach, the validity of the lifetime assessment is limited by the knowledge gaps on materials properties, assumptions made for analysis and the predictive capability of the simulation tools to capture potential failure features. Given that a full proper experimental verification under fusion-relevant loading conditions is virtually not possible, the design-by-analysis approach needs to be considered a complementary design methodology albeit open issues and limitations. In this article, selected critical issues arising in the practice of the design-by-analysis approach are discussed. Particularly, those modelling issues are highlighted which may have a substantial impact on the assessment of structural integrity and lifetime against major failure modes. The potential predictive capability of FEM-based simulation tools is demonstrated. The uncertainties being implicit in the lifetime estimation are illustrated in diverse case studies and the factors affecting estimates are discussed. Finally, outstanding modelling issues needing further clarification are addressed.

Key words: divertor target, high heat flux, DEMO, lifetime, failure, design-by-analysis

*Corresponding author: Jeong-Ha You (you@ipp.mpg.de)

[1]Currently at OSRAM Opto Semiconductors GmbH.

Highlights

- Critical modelling issues arising in the practice of the design-by-analysis approach are presented.
- The impact of these issues on the structural lifetime assessment against major failure modes is studied.
- The factors affecting the lifetime assessment and the resulting uncertainties are discussed.
- The predictive capability of FEM-based simulation tools is demonstrated.

1. Introduction

The divertor target of a nuclear fusion reactor is a plasma-facing component (PFC) contributing to crucial functions of the divertor such as heat removal and particle exhaust during fusion operation. The targets are subjected to a very harsh and complex loading environment characterized by intense particle bombardment, high heat fluxes (HHF), fast neutron irradiation, varying stresses and impact loads [1-5]. Such combined loads may possibly cause premature damage and failure of the components [6-9]. Unfortunately, there is only tenuous knowledge about the synergistic effects of the actual combined loads on the materials and structure of the divertor target during a fusion operation.

For a robust design, the structural integrity must be assured against complex failure modes for the envisaged operation scenarios in order to ensure the required lifetime. To this end, the lifetime against structural failure needs to be estimated by means of either experimental testing (design-by-experiment) or computational analyses (design-by-analysis, design-by-code). In the former approach, a full experimental verification of lifetime is currently not possible because no proper nuclear testing facility (fast neutron irradiation and high heat flux testing on components) is available. In the latter approach, the validity of the lifetime assessment is limited by the knowledge gaps on materials properties, assumptions made for analysis and the predictive capability of the simulation tools to capture potential failure features.

The HHF technology for the ITER divertor target was validated mainly through the design-by-experiment route supported by code-based design studies to take into account irradiation effects [10-13]. This approach may be justified by the fact that the neutron irradiation dose expected for the ITER divertor is relatively low ($\leq$0.5 dpa) so that the irradiation test data obtained from fission reactors could be utilized for specification of design allowables relevant for analysis [14]. This will not be the case for the DEMO divertor since an order of magnitude higher damage dose is expected whereas only few materials data are available for the relevant dose level [5, 15]. At high neutron fluence, adverse effects due to transmutation are expected while the effects due to dpa damage will probably be saturated below 1 dpa [14]. The recent HHF technologies developed for the DEMO divertor were tested only under non-nuclear testing conditions [16-19].

The design-by-code approach will not be fully applicable for the DEMO divertor targets in the near future, as the design code is still under development and not mature enough for use [20]. It surely will take many years until missing materials data are populated and design rules with valid failure criteria are established.

Therefore, the design-by-analysis approach may need to be considered a primary design methodology complementary to the other two approaches. The virtue of the design-by-analysis approach is its capability to deliver a quantitative assessment of lifetime as well as information on failure features for a wide spectrum of operational scenarios. This is particularly useful when an experimental verification becomes impractical.

On the other hand, there are also implicit limitations in the design-by-analysis approach because its practice is subject to modelling assumptions, predictive capability of simulation tools and uncertainties in materials data [21-23]. As the validity of predicted failure features and assessed lifetime is affected by such limitations, the dependence of predicted results on the individual factors affecting the validity needs to be understood. If the limitations should pose a significant consequence in lifetime assessment for a specific failure mode, the case shall be clarified in terms of credibility and caveats.

In this article, a number of practical case studies are presented where the outstanding issues arising in the design-by-analysis practice are discussed and the uncertainties implicit in lifetime assessment are examined. Focus is placed on major failure modes (fracture, fatigue, ratchetting) expected under typical HHF loads and neutron irradiation. The predictive capability of employed FEM-based simulation tools is demonstrated.

2. Geometry, thermal loads and boundary conditions

The preconceptual design of the European DEMO divertor target has been performed in the framework of the dedicated project (WPDIV) of the EUROfusion Consortium [24-25].

The CAD model of the outboard divertor target of the European DEMO reactor is illustrated Fig. 1 (a) [26]. The underlying cassette body is not displayed for brevity. The cooling pipe of the individual target elements are connected to the feeding pipe (blue) and the outlet pipe (dark red) via the coolant distributor and collector manifold, respectively.
A typical part of a target element of the target plate is shown in Fig. 1 (b) [27].

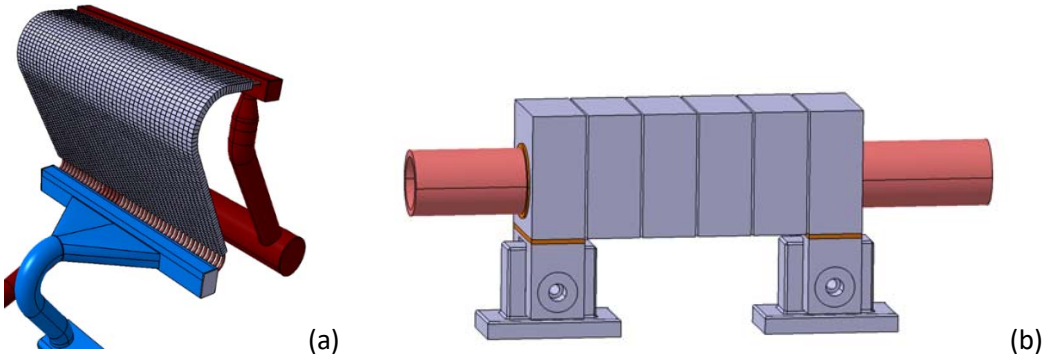

Fig. 1. CAD model of an outboard divertor target of the European DEMO reactor (a) and a typical part of a target element of the target plate (b) [26, 27].

The poloidal profile of the heat flux footprint on the target plate surface is plotted in Fig. 2 in the normalized scale (only the contribution from plasma particles in the scape-off layer is plotted) [28]. The profile exhibits a Gaussian distribution centered around the strike point with the full width at half maximum of about 5 cm. During the stationary operation, the peak heat flux density is expected to reach roughly 10MW/m² (subject to revision) while the heat load outside the strike point location decays rapidly [29, 30].

If a slow transient event occurs, the surface will be exposed to much higher heat flux up to 20-70MW/m² for a wide range of pulse duration [29, 30]. In this circumstance, poloidal sweeping of the strike point shall be activated in order to spread out the heat flux peaking over an extended spatial range with an optimized amplitude and frequency [28].

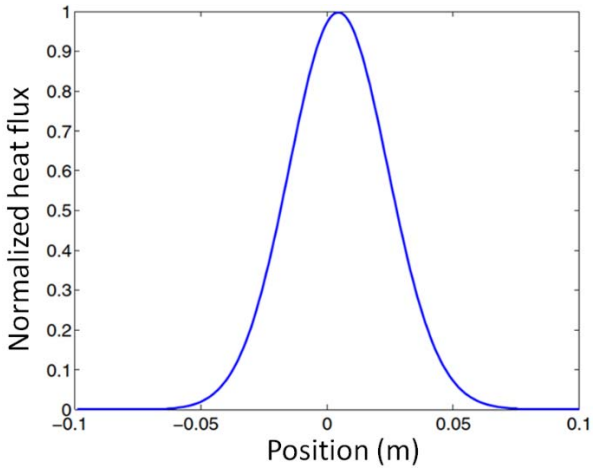

Fig. 2. Assumed poloidal profile of the heat flux footprint on the target plate surface in the normalized scale [28].

The targets are cooled by pressurized water (current baseline) with the inlet temperature of 130°C (at strike point: ≤150°C) and an inlet pressure of 5MPa [31]. The power deposited on the targets is roughly 60MW on average and the coolant temperature rise over the target is calculated to reach 7°C [32, 33]. The cooling condition was determined in such a way that the maximum heat flux on the inner wall of the cooling pipe does not violate the 40% safety margin to the local critical heat flux under the applied surface heat load of 20MW/m² in thermal equilibrium [24, 34].

In WPDIV, the ITER-like divertor target design was adopted as baseline while alternative design concepts were developed in parallel [16, 19]. The ITER-like target design is characterized by an axial array (~1m) of tungsten monoblocks joined to a long cooling pipe made of copper alloy running through the central bore of the blocks. The schematic model of a single monoblock unit is illustrated in Fig. 3. Pure tungsten (hot-rolled) and CuCrZr alloy are the baseline materials used for the blocks and the pipe, respectively. A soft copper interlayer is inserted between the block and the pipe for relieving stresses. The top face of the block is the plasma-facing side. The tungsten block acts as sacrificial armor and the copper alloy pipe as heat sink. The dimensions of the monoblock were optimized for mitigating the driving force to initiate and extend a deep crack at the armour surface [35, 36]. In the HHF testing campaigns conducted for the WPDIV program, no crack was found in any of the 48 mock-ups (360 monoblocks) tested at 20MW/m² to 500-1000 pulses [16-19]. A relatively thick (5-8mm) armor was used to allow a sufficient operational lifetime against erosion loss due to sputtering.

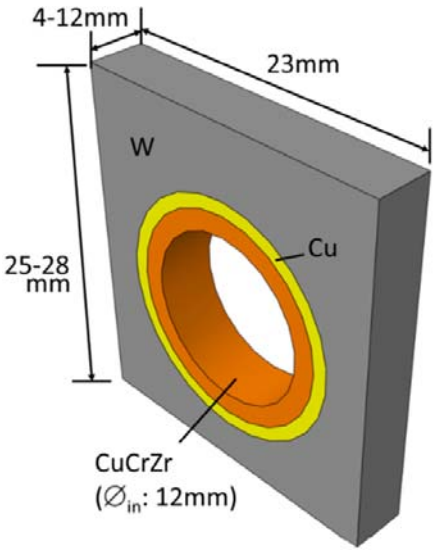

Fig. 3. A schematic illustration of a single monoblock unit of the DEMO divertor target.

Fig. 4 shows two real mock-ups fabricated and used for HHF testing each with a different block dimension (armor thickness: 5mm vs. 8mm, axial thickness: 4mm vs. 12mm) [19]. The current baseline dimension is 12mm×23mm×28mm (armor: 8mm) as shown in the right picture.

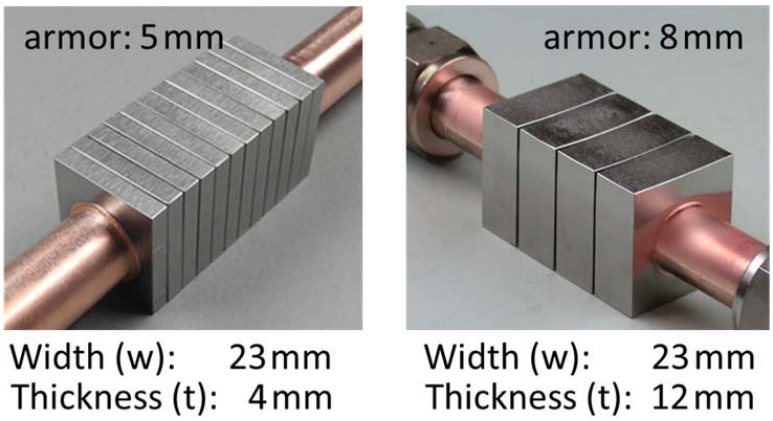

Fig. 4. Two mock-ups fabricated and used for HHF testing each with a different block dimension (armor thickness: 5mm vs. 8mm, axial thickness: 4mm vs. 12mm) [19].

As thermal load, a uniform surface heat flux (either 10MW/m² or 20MW/m²) applied on the armor top face was assumed. A fixed coolant temperature (150°C) and static pressure (5 MPa) was applied on the cooling

pipe inner wall. Cyclic HHF loads with the pulse length of 10s were adopted where a thermal equilibrium was reached (the same as in the real HHF tests). For the low cycle fatigue (LCF) analysis, loading cycles were continued until the response was saturated. For the ratchetting analysis, 300 cycles were simulated. For the creep simulation, a pulse time of 7200s was assumed. The initial residual stress state was considered by including the thermal history of the fabrication process prior to the main HHF loading step. Bending was suppressed by restraining the bottom face. The materials property data used for this study are found in [6-8, 37].

3. Thermal response

Fig. 5 shows the temperature distribution in the target monoblock unit in the thermal equilibrium under the heat flux load at 20MW/m². The steep temperature gradient with the extremely large temperature range building up in the armor and the large mismatch of thermo-elastic properties between the armor and the cooling pipe suggest that substantial thermal stresses are produced. The maximum temperature on the top face reaches 2400°C (homologous temperature: >0.7) whereas the block region around or below the cooling pipe remains below 450°C. The lower half of the irradiated tungsten block remains below the ductile-to-brittle transition temperature (DBTT) even under the HHF load at 20MW/m².

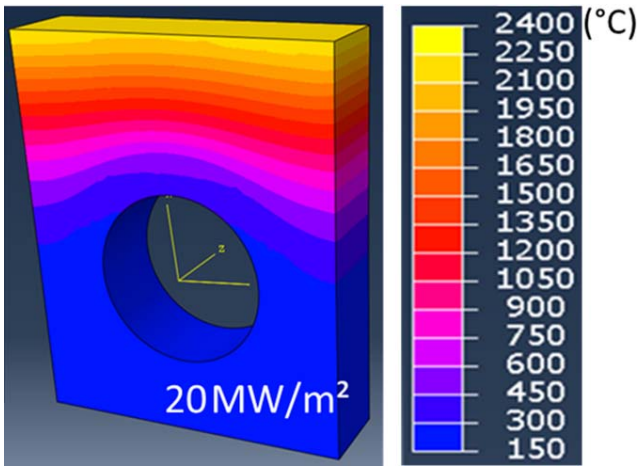

Fig. 5. Temperature distribution in the target monoblock unit in the thermal equilibrium at the heat flux load of 20MW/m².

The material damage features in the hot region will be distinctively different from those of the cold region. The tungsten armor will likely degrade as a result of complex microstructural changes taking place under the interaction between stress, temperature, lattice damage and transmutation products [38]. Use of irradiated tungsten below DBTT is generally deemed undesirable in the PFC community [39].

Fig. 6 shows the equilibrium temperature distribution in the cooling pipe under the applied HHF load at 10MW/m² (left) and 20MW/m² (right). Also in the cooling pipe, a pronounced temperature gradient builds up. Since the cooling pipe serves as structural component, the impact of operational temperatures on the mechanical performance is a critical design concern. Table 1 shows the temperatures at four positions in the pipe under the surface heat flux at 10MW/m² and 20MW/m². The two temperature values of each case correspond to the armor thickness of 5mm and 8mm, respectively. At 10MW/m², the maximum temperature is bounded below 310°C and the lower half part of the pipe is below 190°C. At 20MW/m², the maximum temperature reaches values above 430°C and the entire upper armour part above the pipe is at temperatures higher than 300°C. The lower half part of the pipe is still below 230°C even at 20MW/m².

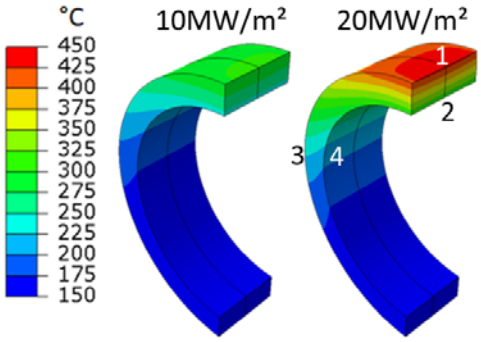

Fig. 6. Temperature distribution in the cooling pipe of the target in the thermal equilibrium under the surface heat flux at 10MW/m² (left) and 20MW/m² (right).

Table 1. Temperatures at four positions in the cooling pipe (as indicated in Fig. 6). Temperatures are given for two armor thicknesses (5mm, 8mm).

	Armor thickness to the top face: 5 - 8mm	
	10MW/m²	20MW/m²
1) Max. temp. at the pipe interface	301 - 306°C	431 - 438°C
2) Max. temp. at the pipe inner wall	240 - 243°C	304 - 308°C
3) Temp. at the side (interface)	187 - 189°C	219 - 223°C
4) Temp. at the side (inner wall)	174 - 176°C	195 - 199°C

Note that CuCrZr alloy undergoes significant softening by microstructural ageing under long-term thermal exposure at temperatures typically above 400°C. The irradiation-induced hardening and embrittlement of CuCrZr alloy begins to disappear in the range 150-200°C by thermal recovery of lattice damages [40]. This means that the lower half of the cooling pipe will remain embrittled and hardened during a whole operation period even including slow transients. The sensitive dependence of CuCrZr alloy properties under simultaneous thermal loads and irradiation requires considerations in terms of design-material interface [41, 42].

4. The cooling pipe

The cooling pipe is classified as structural member as it carries primary loads (coolant pressure and impact force upon disruption). Together with the attachment units for target fixation, the cooling pipe contributes to the structural stability of the entire target system. As such, the cooling pipe design should fulfill structural design rules. The initiation and evolution of a structural failure is governed by the stress states, temperature, strain history and the actual state of the material. Hence, the thermal history and the material state assumed for analysis may affect the results of design rule application. In this section, selected issues related to this aspect are discussed.

4.1. Initial residual stress

Joining of the armor blocks to the cooling pipe at an elevated temperature produces residual stress due to the mismatch of differential thermal strains between the dissimilar materials. In the case of the ITER-like design, hot radial pressing (HRP) technique was adopted where the parts were joined at 580°C for 2 hours and cooled down uniformly to the ambient temperature. This cooling step should be considered as a part of the entire thermal history for stress calculation. The residual stress defines the initial stress state onto which the thermal stress produced by the subsequent HHF loads is superposed. The challenge is that calculating the residual stress is not trivial because the viscous stress relaxation occurring in the joining process is not well known. Analysts have two options:

1) to use a realistic (but complex) visco-plastic constitutive model for direct simulation of the relaxation process taking the joining temperature as actual stress-free temperature (ASFT)

2) to use a simplified (but less realistic) plasticity model omitting the viscous term while the stress relaxation is compensated via an adjusted temperature difference defined by effective stress-free temperature (ESFT).

The validity of the former option depends on the availability of a proper constitutive equation and material parameters for creep. The feasibility of the latter approach relies on the accurate specification of an ESFT. The exact ESFT could be experimentally calibrated by means of nondestructive methods (X-ray or neutron diffractometry) using a reference joint specimen fabricated by the same joining process. The specification of an ESFT may have a big influence on the initial as well as subsequent stress states under HHF loads. This problem is clearly demonstrated in Fig. 7 where the stress evolutions under the HHF load of 20MW/m² are plotted for the two limiting cases of ESFT, namely, 580°C (null relaxation) and 20°C (perfect relaxation). The position of the plotted stress states (left: hoop component, right: axial component) is at the uppermost region of the pipe (axial thickness: 12mm). The joining step (from 580°C to RT) and the preheating step (from RT to 150°C) were hypothetically squeezed within the first 2 seconds. The real stress state should be somewhere between these two liming cases.

The hoop stress is fully shifted from the tensile to compressive regime when the relaxation fully erases the thermal stress due to CTE (coefficient of thermal expansion) mismatch. However, the stress amplitude itself remains unaltered. The axial stress exhibits an opposite trend upon relaxation where the stress state is only partially shifted from compressive to tensile preserving the stress amplitude. In the case of the hoop stress, the full reversion of stress sign from tensile to compressive is beneficial since only tensile stress contributes to crack growth in a non-ductile fracture. When stress relaxation fully comes into effect (ESFT: 20°C), the entire hoop stress range remains compressive and the stress almost vanishes in the cold state minimizing the failure risk by a radial crack. Thus, the hoop stress variation without creep relaxation (ESFT: 580°C) represents the most critical situation with the highest tensile stress in the cold state.

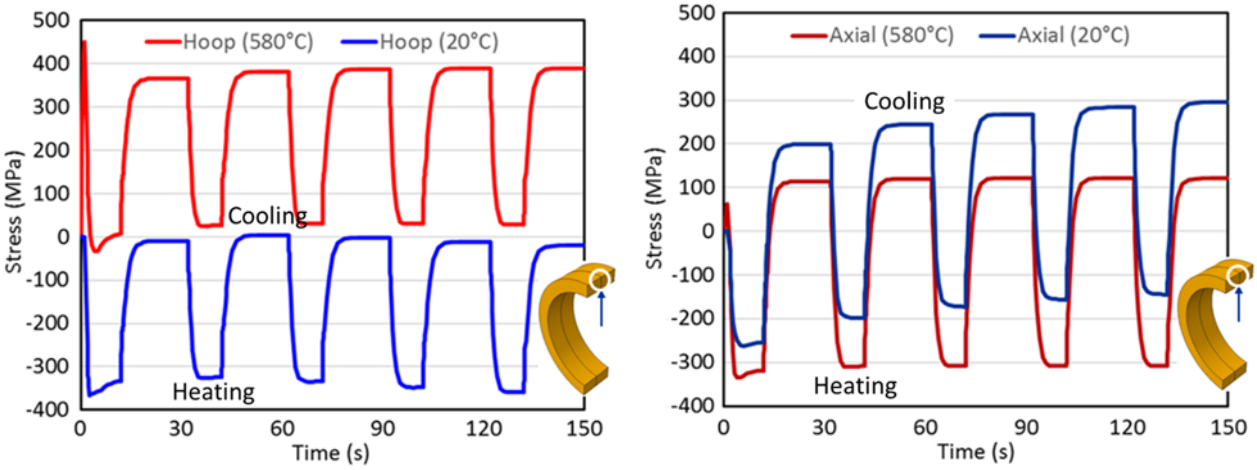

Fig. 7. Stress evolution (left: hoop, right: axial) at the uppermost position of the pipe (axial thickness: 12mm) under cyclic HHF loads (20MW/m²) calculated for two limiting cases of ESFT: 580°C (null relaxation) and 20°C (perfect relaxation). The joining and the preheating step was hypothetically squeezed in the first 2s.

Given the uncertainty of an ESFT and its strong impact on stress as shown in Fig. 7, a direct simulation of relaxation effects in the joining step may allow a more definite interpretation. Unfortunately, there are only a few material data available in the literature for creep modelling of CuCrZr alloy. In [43], material parameters for the secondary creep stage of CuCrZr alloy are presented based on the Norton-type creep model (see Fig. 8). Using the data, residual stress of the pipe was calculated for the HRP joining process (580°C, 2h). Fig. 9 shows the residual hoop stress calculated with creep relaxation (right). For comparison, the stress calculated without relaxation is also given (left). Surprisingly, the stress states of both cases are almost indistinguishable. This indicates that the secondary creep stage made a negligible contribution to

stress relaxation. To capture the whole relaxation process, the missing contribution from the primary creep stage needs to be included. Unfortunately, no literature data of primary creep is available for CuCrZr alloy presently. Thus, a unified visco-plastic constitutive equation capable of covering the primary as well as the secondary creep stage can not be constructed for CuCrZr alloy.

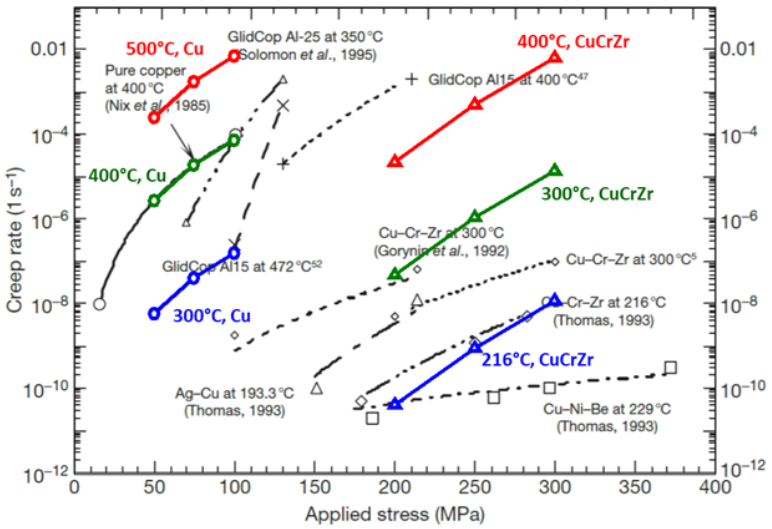

Fig. 8. Creep strain rates (in the secondary creep stage) of copper and copper base alloys [43].

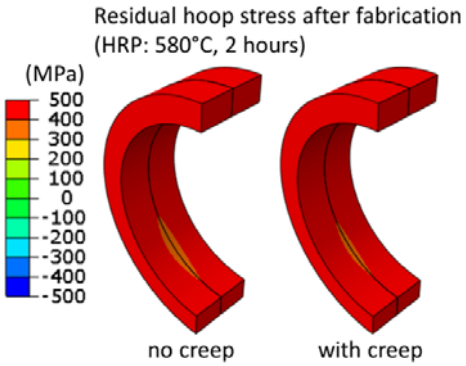

Fig. 9. Residual stress states (hoop component) from the HRP joining process calculated with (right) and without (left) creep relaxation.

4.2. Elastic shakedown

It is well known that the presence of a residual stress field is likely to lead to an elastic shakedown response of an elasto-plastic structure under variable loads [44, 45]. In an elastic shakedown state, a structure exists in a purely elastic state even though the stress state continues to vary within a predefined loading space. The plastic strains cease to increase after a certain amount of accumulation. This phenomenon is particularly beneficial for a complex structure under variable loads because failure modes due to plastic strain damages (e.g. LCF) can be excluded.

Fig. 10 shows the evolution of the three principal plastic strain components at the upper inner wall of the cooling pipe during the first five cycles of HHF pulses at 20MW/m² (monoblock axial thickness: 12mm). As in Fig. 7, two limiting cases of ESFT are compared (580°C: null relaxation, 20°C: perfect relaxation). If no relaxation occurs (ESFT: 580°C), plastic strains of a significant amount (0.5-1%) have been produced during the joining step prior to the HHF loading. However, the plastic straining readily ceases to increase upon the subsequent HHF loading being saturated already in the first cycle. This feature manifests an elastic shakedown. A similar shakedown behavior is also found for the case of perfect relaxation (ESFT: 20°C). The rapid elastic shakedown response of the cooling pipe seems due to the initial residual stress state coined

by the extensive plastic deformation during either the joining process (580°C) or the first HHF loading cycle (20°C). In case such an elastic shakedown state prevails in the pipe, a LCF failure can be excluded. The shakedown state can be broken down if the original yield stress (and flow stress) drastically decreases as a result of thermal softening or microstructural ageing under long-term thermal exposure.

The same elastic shakedown behavior is found for the cooling pipe with the axial thickness of the W armor block of 4mm (see Fig. 11).

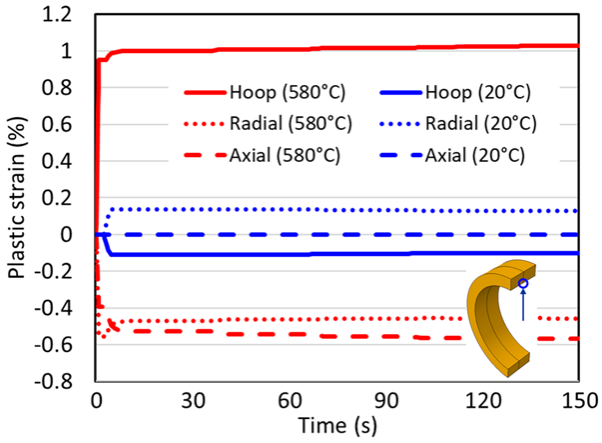

Fig. 10. Plastic strain evolution at the upper pipe inner wall under cyclic HHF loads (20MW/m², 5 pulses) calculated for two limiting cases of ESFT: 580°C (null relaxation) and 20°C (perfect relaxation). The strains were calculated without creep relaxation (block axial thickness: 12mm). The joining step was hypothetically squeezed in the first 1s.

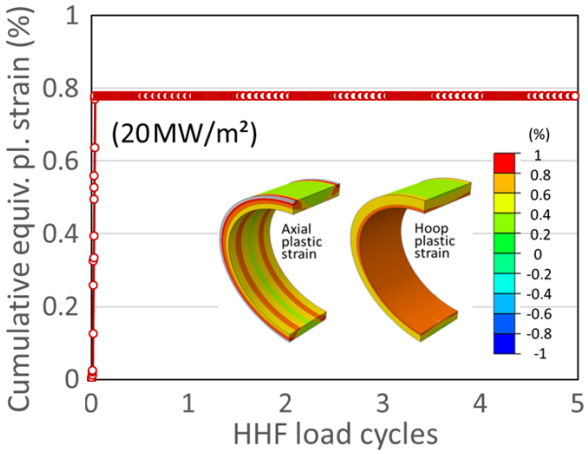

Fig. 11. Cumulative equivalent plastic strain evolution at the upper pipe inner wall under cyclic HHF loads (20MW/m², 5 pulses) calculated for ESFT of 580°C (block axial thickness: 4mm). The joining step was hypothetically squeezed in the first 1s.

4.3. Stress-temperature phase offset

The cyclic variation pattern of the hoop stress (at the uppermost region) in Fig. 7 indicates that the stress state can evolve either in-phase (ESFT: 20°C) or out-of-phase (ESFT: 580°C) mode with the temperature variation depending on the initial stress state. The out-of-phase loading stands for the situation where stress reaches the maximum (in magnitude) when the thermal load is off while it relaxes to the minimum when the thermal load is on. The in-phase loading depicts the opposite situation. Note that the trends of phase relationship in Fig. 7 are only valid for a specific position (the uppermost region). At different locations, a deviating phase relationship may occur.

Fig. 12 shows the distribution of the hoop stress states in the pipe under HHF loads (left: 10MW/m², right: 20MW/m²) and cooling (150°C) for the ESFT of 580°C. The pipe shows a similar stress behavior for both HHF loads over the entire heating-cooling cycle apart from the minor difference in stress intensity. The uppermost region experiences the highest tensile stress (~400MPa) during the cooling phase (150°C) while the stress is completely relaxed upon the HHF loading. The lower part (≤ 200°C) experiences considerable tensile stresses (≤270MPa) during the HHF loading while being relaxed upon cooling. This indicates an in-phase stress variation with the temperature (ESFT: 580°C).

CuCrZr alloy is strongly embrittled by neutron irradiation at a lower temperature (<150°C). In those regions of the pipe where critical tensile stresses appear at a local temperature below 200°C, a brittle failure may occur due to exhaustion of ductility [23]. Fig. 12 shows that tensile hoop stress prevails mostly in the 'cold' state (≤150°C). The tensile hoop stress is responsible for the K_I mode growth of a radial crack in the pipe. The structural integrity against the corresponding failure criteria (fast fracture, fatigue fracture) needs to be assessed [23].

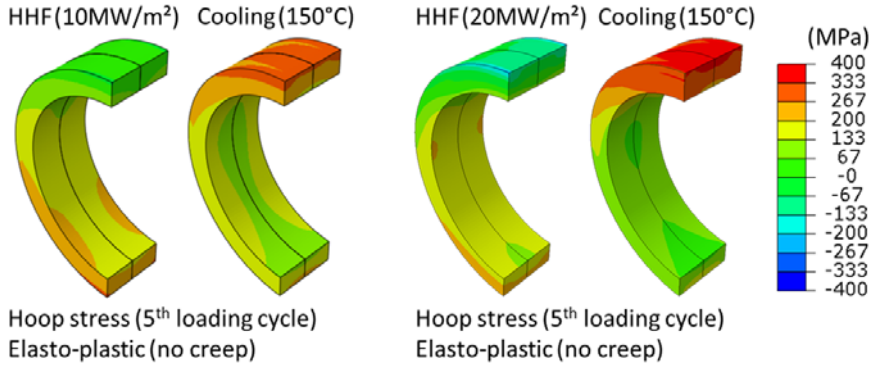

Fig. 12. Stress states in the cooling pipe during the HHF loading and the subsequent cooling phase (150°C), respectively (left pair: 10MW/m², right pair: 20MW/m²). Plotted is the hoop stress after five HHF pulses. (elasto-plastic simulation without creep).

The long-pulse operation (2 hours) of DEMO can cause creep of the cooling pipe provided the temperature and stress is high enough during a stationary operation. Fig. 13 shows the distribution of (equivalent) creep strains in the pipe under the stationary HHF load at 10MW/m² at the first and the 5th loading cycle (pulse length: 2h). The creep strain states after the HRP joining process (580°C, 2h) are also shown for comparison. In the joining step, moderate creep strains (1.2-1.6%) were produced in the bulk of the pipe with local hot spots (~2%) on the inner wall. Creep strain increased substantially (1.4-2.0%) already after the first pulse with an extensive hot spot area (~2.2%) on the inner wall. Analogous to the plastic strain behavior, the creep strains were mostly saturated after the first pulse.

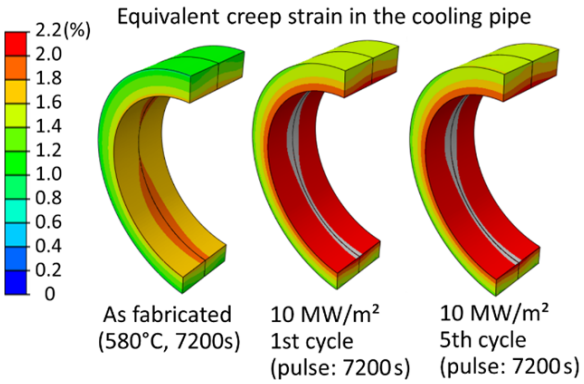

Fig. 13. Equivalent creep strain in the cooling pipe under the stationary heat flux of 10MW/m² at the first and the 5th loading cycle (pulse: 7200s).

Such a substantial creep leads to a considerable relaxation of the thermal stress. Fig. 14 shows the stress states calculated with the secondary creep at the first (left pair) and the 5th loading cycle (right pair) of HHF load at 10MW/m² and cooling at 150°C. Comparison of Fig. 14 with Fig. 12 manifests that the creep during the HHF loading indeed caused significant stress relaxation resulting in a notably reduced residual stress in the cooling phase. The creep relaxation is beneficial in the sense that the driving force for a brittle failure is mitigated. Furthermore, a creep rupture will be hardly probable because the detrimental tertiary creep stage will not set in under the given strain-controlled load (by thermal strain mismatch) owing to stress relaxation.

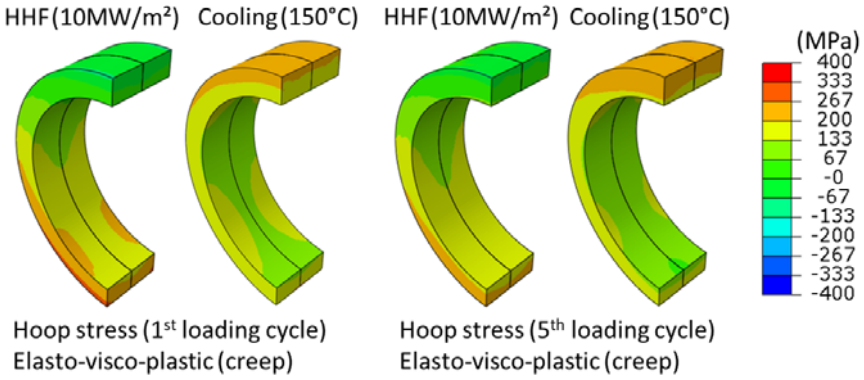

Fig. 14. Stress states of the cooling pipe at the first (left pair) and the 5th loading cycle (right pair) each for the heating (10MW/m²) and the cooling phase (150°C). (Pulse duration: 2h)

4.4. Softening by thermal ageing

Precipitation-hardened CuCrZr alloy is known to lose its initial yield strength by ageing under a long-term thermal exposure at an elevated temperature [15]. One of the design concerns is the possibility that the yield stress of the pipe drops due to thermal excursions produced by repeated slow transient events. Under HHF load of 20MW/m², the pipe bulk temperature exceeds the allowable service temperature limit (~350°C). If the cumulative time of the intermittent thermal excursions is long enough to activate microstructural ageing (mainly Ostwald ripening of precipitates), the pipe undergoes permanent softening. As discussed in section 4.1, the elastic shakedown state disappears and LCF begins to develop once excessive softening progresses extensively.

In order to assess the impact of softening, an extreme case was investigated where a complete loss of yield stress was assumed. For this, the yield stress of soft copper was used for the cooling pipe and a cyclic HHF loading at 20MW/m² was simulated. The saturated plastic strain amplitude at the fifth pulse was taken to calculate the LCF life. Fig. 15 shows the distribution of accumulated equivalent plastic strains on the axial cut section of the pipe and the interlayer as illustrated in the schematic drawing. It is remarkable that the plastic strain is highly localized (7-31%) in a small region ($\leq 0.5\times0.5$mm²) near the free surface edge of the pipe-to-interlayer bond interface. The remaining region experiences mostly moderate plastic strains ($\leq 6\%$) although the yield stress was very low (3MPa). The estimated LCF life of the strain hot spot region ranges roughly from 5950 to 9730 cycles at 10MW/m² and from 740 to 1860 cycles at 20MW/m². These numbers represent the most conservative prediction.

The pronounced heterogeneity in the plastic strain distribution characterized by the local hot spot poses a complication with respect to the question as to how to define a LCF life of the pipe. In the code rules, a LCF life is defined as the number of load cycles to the onset of global failure (e.g. reduction of stress range to the half of the initial value) where a uniform strain profile is assumed over the cross section of a critical part. In the case of a highly non-uniform strain distribution, the LCF life will be different from position to position depending on local strain amplitude. The LCF life calculated for the strain hot spot with a large amplitude gives obviously a conservative estimate valid only for the hot spot [22]. Thus, the LCF life at the hot spot (with the largest amplitude) should be interpreted as the number of cycles up to the onset of fatigue crack initiation. Beyond the LCF regime (i.e. after crack initiation), fatigue fracture determines the ultimate

failure. The failure life in this regime is determined by the cyclic crack growth rate and the amplitude of the stress intensity factor (ΔK_I) at the crack tip [46].
From the fact that the fatigue life predictions in Fig. 15 indicate the life only up to the crack initiation in the fully softened material state, it can be concluded that the thermal ageing of the pipe (no matter how much it is) will not lead to a premature failure earlier than the specified number of transient events (≤1000 times).

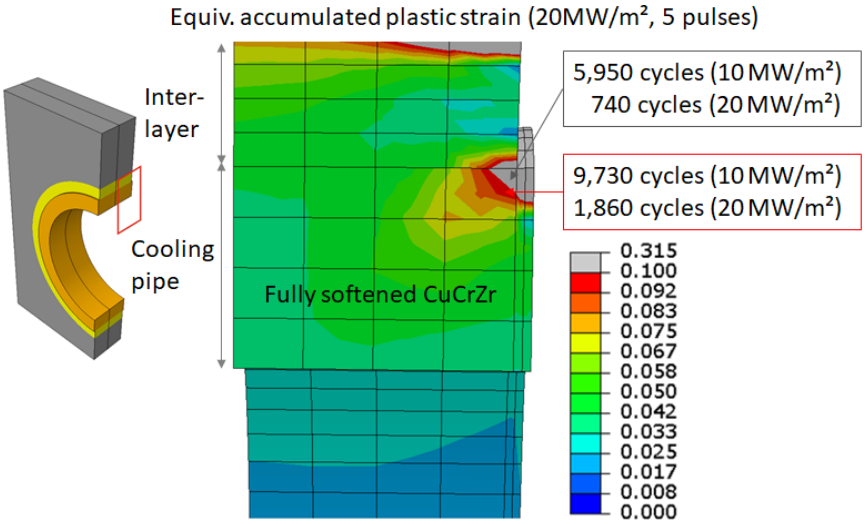

Fig. 15. Distribution of accumulated equivalent plastic strain on the axial cut section of the pipe and the interlayer after the fifth pulse of cyclic HHF loading at 20MW/m² (left). The estimated LCF lifes of the strain concentration region are given in the boxes for the HHF load of 10MW/m² and 20MW/m².

4.5. Coolant temperature and embrittlement

As discussed in section 4.3, the combination of high tensile stress and low temperature (≤150°C) poses a potential risk of brittle fracture for the embrittled pipe because the uniform elongation drops to ≤1% [40]. The temperature in the 'cold' state is determined by the coolant temperature (baseline: 130-140°C). Operating at a higher coolant temperature (say, 200°C) will surely mitigate this problem. Fig. 16 presents literature data of temperature dependent total elongation of irradiated and un-irradiated CuCrZr alloy [13]. The data indicate that the coolant temperature at ≥130°C ensures that the total elongation remains larger than 5% everywhere in the pipe. According to the FEM analysis, the maximum tensile strain was far less than 5%. This means that even though the current operation condition does not satisfy the failure criterion based on uniform elongation, it would pass the failure criterion based on total elongation [23].

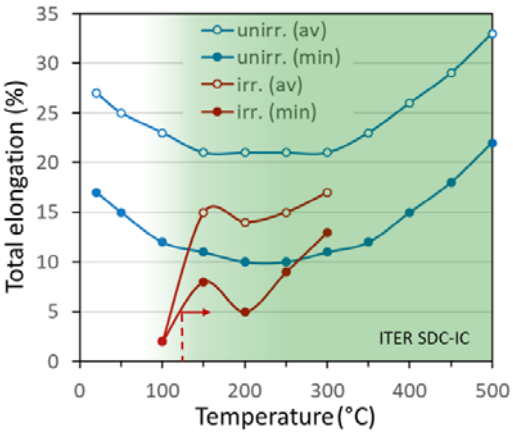

Fig. 16. Temperature dependence of the total elongation (in %) of irradiated and un-irradiated CuCrZr alloy plotting the average and minimum test data [13].

From the heat exhaust point of view (the primary function of divertor target), operating the targets at a lower coolant temperature (say, 100°C) is obviously advantageous because the margin to the critical heat flux is proportionally increased [24]. Of course, this benefit is compromised by the embrittlement issue. This trade-off could be compensated if a fracture mechanics-based design rule is employed. This idea is motivated by the finding that the toughness of irradiated CuCrZr alloy increases as temperature decreases.

Fig. 17 shows the literature data of measured critical fracture energy (J_Q data) of irradiated and un-irradiated CuCrZr alloy [13]. Also plotted are two predicted ranges of strain energy release rate (J integral) at the tip of a radial crack (0.5mm, rectangular shape) located at the upper inner wall of the pipe as illustrated. The ranges indicate the crack tip loading during HHF loading (20MW/m²) and cooling (150°C), respectively. The area of the ranges include the safety factor of 3. It is seen that the predicted J integral ranges (incl. the safety factor) are far below the critical values in the cooling phase whereas a slight overlap seems possible during the HHF loading owing to the rapid decrease of toughness with increasing temperature in embrittled state. This indicates that increasing the coolant temperature reduces the margin of stress intensity factor to the toughness of the embrittled pipe. The margin is eventually exhausted if the temperature at the uppermost pipe wall exceeds 350°C. Note, however, that this is a conservative estimation because a rather big crack size (0.5mm) and a hypothetical rectangular (instead of a natural elliptical) crack shape was assumed. For a smaller crack size, the crack tip loading is drastically reduced (see Fig. 18). For instance, when the crack size is reduced from 0.5mm to 0.2mm, the J-integral decreases by a factor of 3.
Recalling that the critical tensile stress states appear in the cold state (in the uppermost region in the cooling phase or in the bottom region during the HHF loading), the high toughness in the lower temperature range below 150°C justifies the operation with the low-temperature coolant (130-140°C).
On the contrary, the drastic drop of the toughness in the higher temperature range clearly highlights the risk of fast fracture during heating in a slow transient event (20MW/m²) even though the tensile stress of the upper part is quite modest (~100MPa). At 10MW/m², the margin to the toughness becomes larger since the temperature range of the upper part is shifted to 250-300°C.

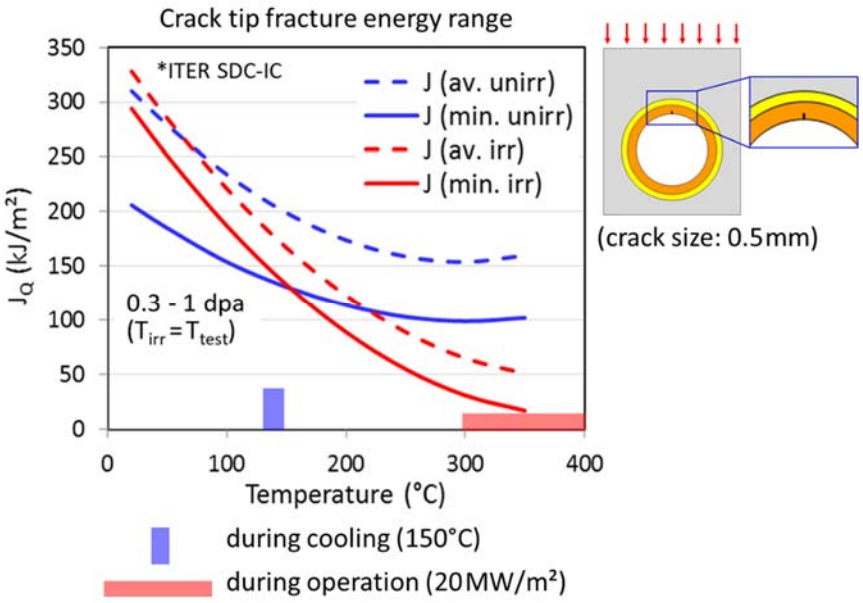

Fig. 17. Measured fracture energy (J_Q data) of irradiated and un-irradiated CuCrZr alloy [13]. Also plotted are expected ranges of strain energy release rate (J integral) at the tip of a radial crack (0.5mm, rectangular shape) located at the upper inner wall of the pipe. The ranges indicate the crack tip loading during HHF loading (20MW/m²) and cooling (150°C), respectively (safety factor: 3).

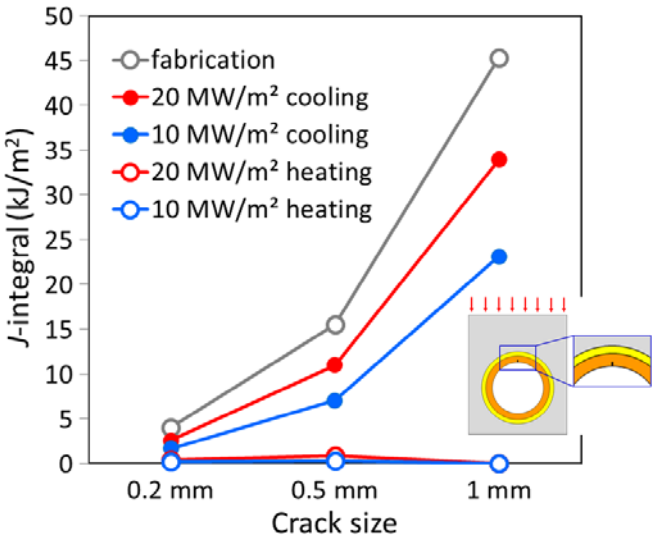

Fig. 18. Strain energy release rate (J integral) at the tip of a radial crack (rectangular shape) located at the upper inner wall of the pipe under HHF loading (10MW/m², 20MW/m²) and cooling (150°C), respectively.

5. Copper interlayer

Although the copper interlayer is not classified as structural member, its mechanical stability is an essential prerequisite for maintaining the global integrity and functionality of the entire target. In this context, the structural failure features of the interlayer should be handled on the same footing as the cooling pipe. Owing to the very low yield stress of soft copper at elevated temperatures, the interlayer undergoes cyclic plastic deformation. As a result, it is prone to LCF and ratchetting. Thus, critical analysis issues are mostly related to cyclic plasticity.

5.1. Strain concentration and fatigue life

One pronounced feature of the deformation behavior is the strong concentration of plastic strain in the local regions near the free surface edge of the bond interfaces as illustrated in Fig. 19. Plotted is the distribution of accumulated equivalent plastic strain in the copper interlayer (a symmetry half) after 300 pulses of HHF load at 20MW/m² (axial thickness: 4mm). Estimated fatigue life values at two selected positions (middle, free edge) are given in the boxes for the HHF load of 10MW/m² and 20MW/m², respectively. A Manson-Coffin type equation was used to calculate the LCF life [6, 35]. The predicted fatigue life differs from each other by an order of magnitude depending on the positions.

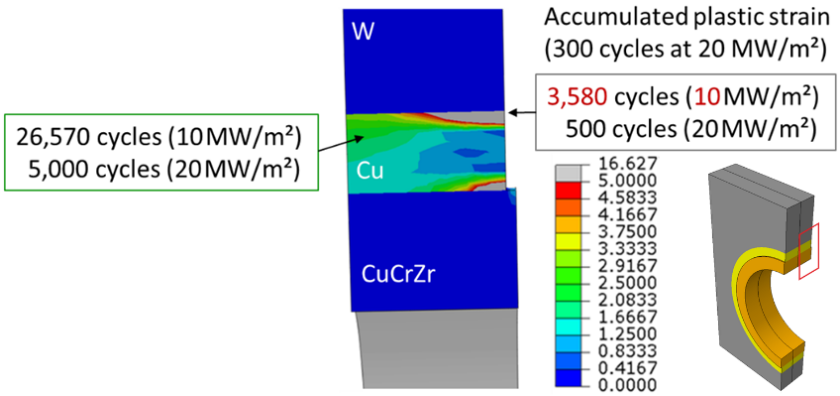

Fig. 19. Distribution of accumulated equivalent plastic strain in the copper interlayer (a symmetry half) after 300 pulses of HHF load at 20MW/m². Estimated fatigue life values at two selected positions are given in the boxes for the HHF load of 10MW/m² and 20MW/m², respectively (axial thickness: 4mm).

LCF life is determined by the amplitude of the principal plastic strain components. In practice, the increment of cumulative equivalent plastic strain (a suitable combination of the principal components of strain tensor) is used as a scalar measure to be compared with uniaxial test data. The increment of cumulative equivalent plastic strain at the middle and free edge region in Fig. 19 is 0.15% and 0.47% under 10MW/m², respectively [35]. It may seem intuitively obvious that the region of plastic strain concentration would experience larger strain amplitudes in proportion to magnitude.

Interestingly, this correlation is not generally valid. Fig. 20 shows the variation of plastic strain components in the interlayer (axial thickness: 12mm) in the uppermost region over the first 10 load cycles at 20MW/m². Plotted are the strain variations at three locations: (a) middle, (b) free edge at 0.1mm below the armor, (c) free edge at 0.3mm below the armor. As expected, the free surface edge region (b, c) exhibits substantially larger strains in magnitude (axial and radial component) compared to the middle region (a). However, the strain amplitudes in the free edge region (hot spot) depend strongly on the vertical position. It is not clear how the combination of the magnitude and the amplitude of plastic strains affect the resulting fatigue life in the tri-axial strain state. The sign of the strain components should play a major role as well.

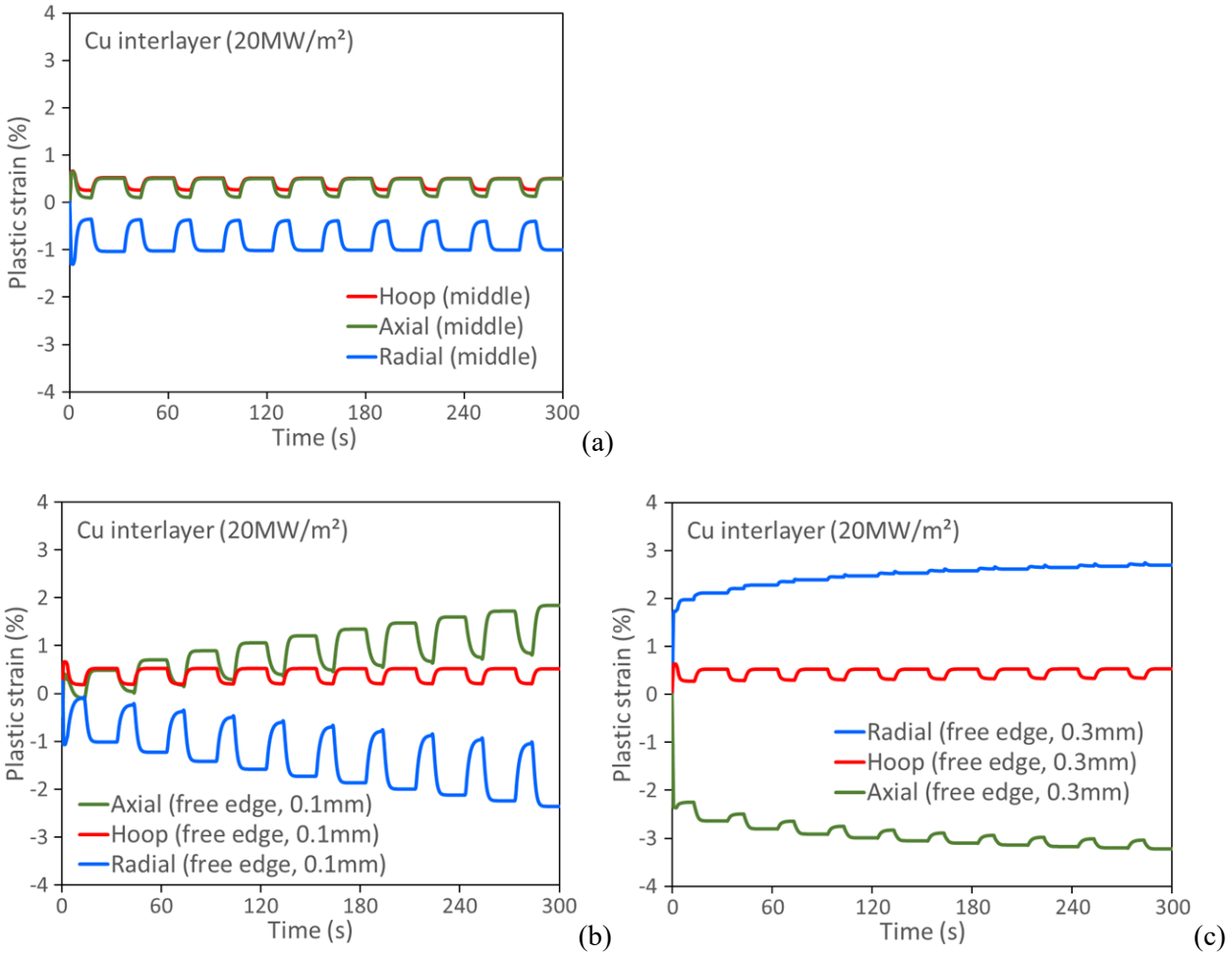

Fig. 20. Variation of the principal plastic strain components (cylindrical coordinate system) at three different locations (a: at the middle position, b: free edge at 0.1mm below the armor, c: free edge at 0.3mm below the armor) over the first 10 load cycles at 20MW/m² (axial thickness: 12mm).

Fig. 21 shows the distribution of three plastic strain components in the copper interlayer after 10 pulses of heat load at 20MW/m². The strain fields in the free surface edge region exhibit a strong concentration and a distinct contrast between the axial and radial component.

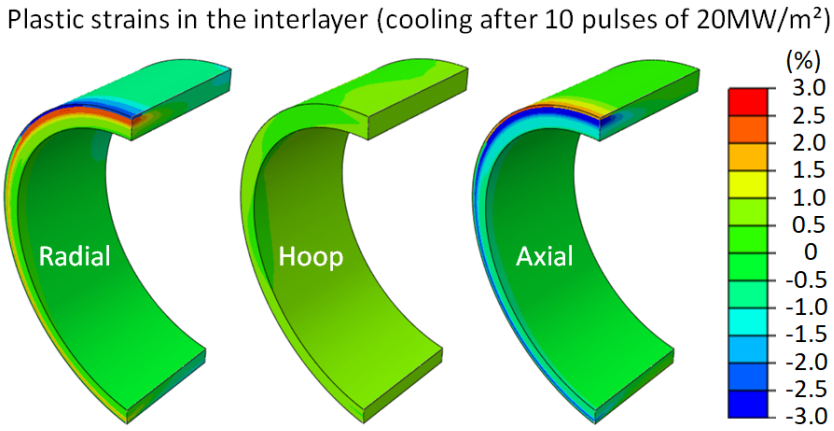

Fig. 21. Distribution of three plastic strain components in the copper interlayer after 10 pulses of heat load at 20MW/m².

The pronounced strain concentration in the free edge region and the strong dependence of the LCF behavior on the strain amplitude raise an outstanding issue as to what region of the interlayer should be selected as a representative location for predicting the LCF life. Actually, this question is related to the definition of LCF life in the presence of a singular strain hot spot. As discussed in section 4.4 for the similar situation of the fully softened cooling pipe, the LCF of the soft interlayer can be defined as the number of loading cycles up to the initiation of a mesoscopic fatigue crack at the free surface edge. In order to specify the fatigue life to the ultimate global failure, a subsequent fatigue fracture life needs to be defined in terms of a cyclic crack growth rate (da/dN) and ΔK_I. A microscopic scrutiny of detailed damage characteristics after a HHF test is useful for understanding the nature of damage and failure mechanism [19]. A non-destructive inspection using ultrasound echo also gives a visible evidence of free edge concentration of fatigue damage as predicted in Fig. 22 [47, 48]. The ultrasonic scan image after 500 pulses of HHF load at 20MW/m² reveals that the free edge hot spot region with mature LCF damages remained confined within a narrow band.

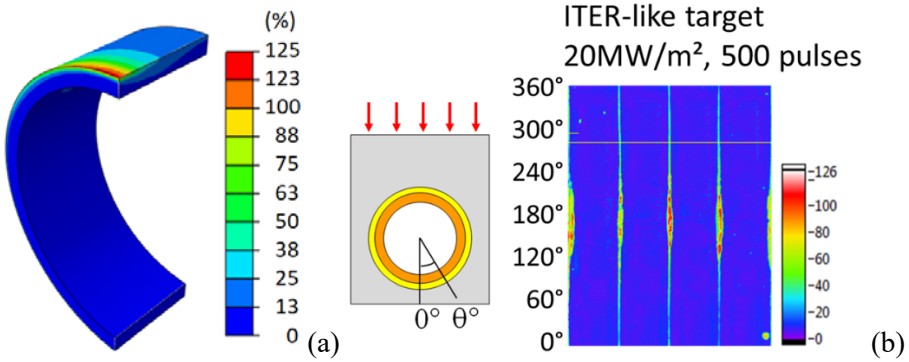

Fig. 22. (a) Distribution of the accumulated equivalent plastic strain in the copper interlayer after 10 pulses of heat load at 20MW/m², (b) Ultrasound echo reflectometry image scanned along the polar coordinates on the pipe inner wall (echo signal detected from the Cu interface/CuCrZr pipe interface: C-scan) [47, 48].

5.2. Ratchetting

Another notable feature is found in the long-term cyclic evolution of plastic strains in the interlayer. Fig. 23 shows the variation of the three plastic strain components (principal strains) at a position in the vicinity of the strain hot spot under HHF load at 20MW/m² (left: first 10 loading cycles, right: 300 cycles). In the initial stage of the cyclic HHF loading, the radial and axial component of the plastic strain increases rapidly from cycle to cycle until roughly 100 cycles and becomes stabilized. The strain amplitude remains nearly constant indicating that the LCF life per se should not be affected by this progressive straining. On the contrary, the hoop component exhibits a gentle monotonic decrease with a minor change in the magnitude.

The substantial increase of the plastic strains continuing over the first 100 cycles clearly suggests that the long-term response needs to be analyzed until saturation. The transient phase (up to 100 cycles) indicates a ratchetting behavior. By definition, a ratchetting leads to an incremental plastic instability. In the present situation, however, the initial instability is bounded by the following saturation in terms of total extent. The negative sign of the axial strain implies a compressive deformation (axial contraction) probably caused by the bending of tungsten armor (due to the inelastic expansion of the top surface layer under the slow transient HHF loads). As the growth of progressive cyclic plastic deformation is eventually limited, the ratcheting is deemed a subcritical concern.

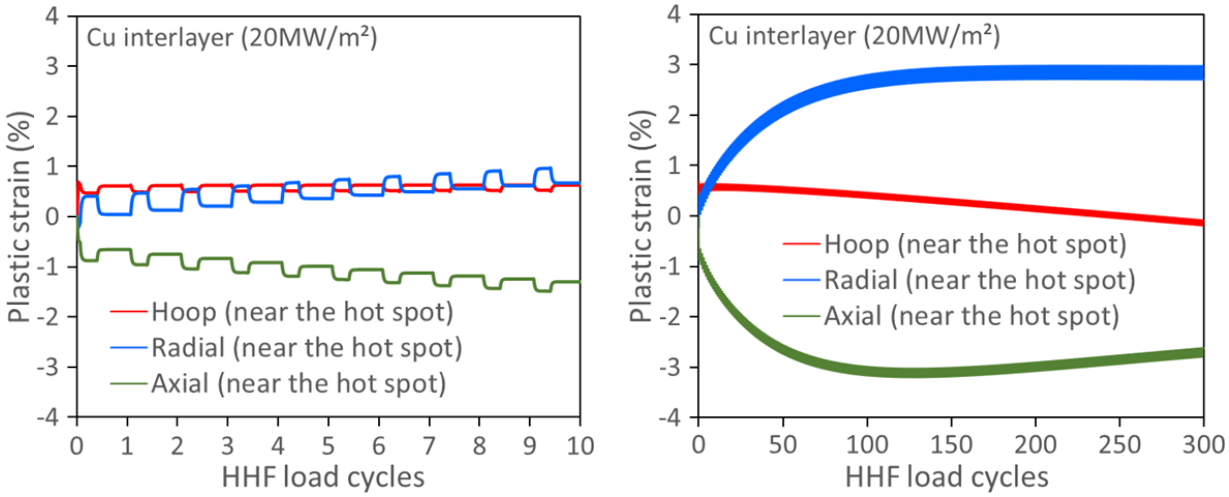

Fig. 23. Variation of the three plastic strain components (principal strains) at a position in the vicinity of the strain hot spot under HHF loading at 20MW/m² (left: first 10 loading cycles, right: 300 cycles).

5.3. Embrittlement due to irradiation

The LCF and ratchetting behavior discussed in sections 5.1 and 5.2 is a unique consequence of cumulative cyclic plasticity. The highly pronounced LCF and ratchetting feature of the interlayer is attributed to low yield/flow stress and high ductility of soft copper at elevated temperatures. A change in yield/flow stress or ductility may alter the original LCF and ratchetting response. This possibility needs to be taken into account in case irradiation effects (hardening, embrittlement) are considerable. In literature, strong embrittlement of pure copper due to irradiation of fast neutrons at elevated temperatures was reported as presented in Fig. 24 [49]. The data show that the total elongation drops nearly to zero at ≥300°C when irradiated at a similar temperature. Unfortunately, this critical temperature range exactly overlaps with the operation temperature of the copper interlayer at the strike point. In [49], the full loss of ductility was attributed to the segregation of helium bubbles (originating from transmutation reactions) at grain boundaries. As the gas bubbles cannot be easily removed by annealing, embrittlement becomes permanent.

The embrittled (and hardened) copper interlayer will behave as linear-elastic material. Stress relaxation by plastic yield will not take place. This response is predicted in Fig. 25 where the hydrostatic stress states of the target is compared between two cases (embrittled vs. ductile interlayer). The comparison shows that the embrittlement indeed leads to substantially higher stresses (tensile in the armor and compressive in the interlayer) while the cooling pipe is little affected. Although the structural part (pipe) is hardly affected by embrittlement, the higher tensile stress intensity in the armor may cause a crack formation at or near the bond interface leading to a local reduction of heat conduction. Cracking of armor blocks in the absence of a stress-relieving soft interlayer was indeed observed in previous HHF tests and explained by simulation [50, 51].

The production and accumulation of helium bubbles increases (approximately linearly) with neutron fluence. Thus, it takes time until the bubble formation at grain boundaries reaches the critical population resulting in complete embrittlement. Therefore, the life usage of the interlayer due to the cumulative LCF damage by

cyclic plasticity will be applicable mainly for the early phase of operation before the occurrence of helium-induced embrittlement. The gradual change of ductility and yield stress poses an additional computational difficulty in lifetime assessment.

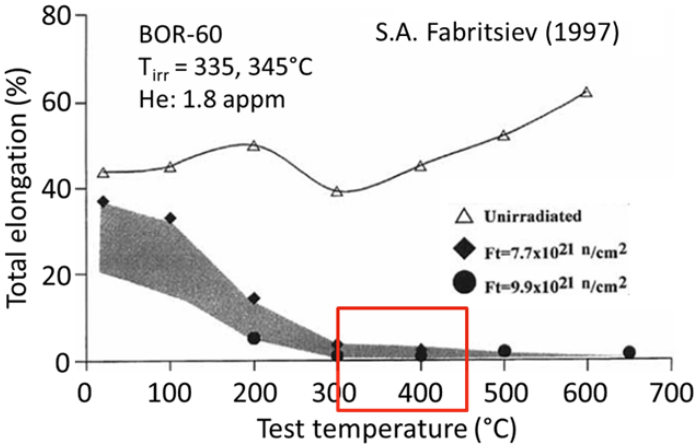

Fig. 24. Total elongation of fast neutron-irradiated pure copper at different test temperatures [48].

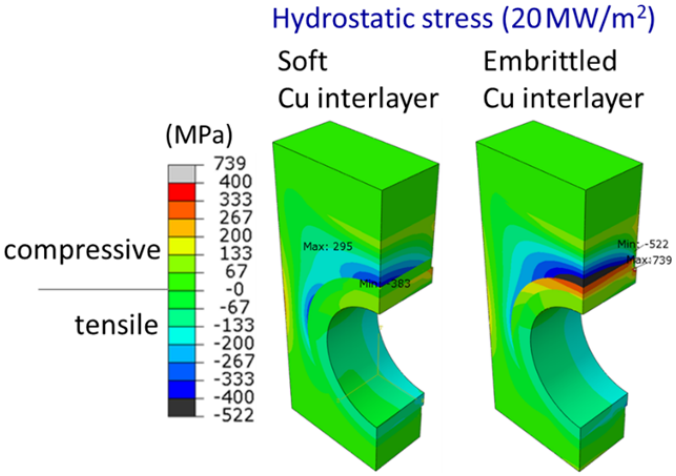

Fig. 25. Hydrostatic stress states of the target compared between the cases of the embrittled (right) and the ductile (left) interlayer (under 20MW/m²). The minus sign denotes tensile stress.

6. Tungsten armor block

6.1. Impact of irradiation

Although not being a structural member per se, the intactness of the tungsten blocks as plasma-facing armor is important for keeping the essential functionality as sacrificial armor. Thus, a holistic approach is required for a global lifetime assessment also taking the failure of the armor blocks into account.

Fig. 26 shows the hoop stress states in a target monoblock unit. Plotted are the stress states after fabrication, under HHF load at 20MW/m² (1st and 5th cycle) and during cooling at 150°C (1st and 5th cycle), respectively. The block dimensions are 28×23×12mm^3 (armor thickness: 8mm). Fig. 27 shows the corresponding crack formation pattern predicted by XFEM tool using ABAQUS code [52]. Crack initiation was determined by the maximum principal stress criterion (assumed tensile fracture stress: 500MPa). Damage evolution (crack growth) was simulated based on an energy-based cohesive traction separation law where the scalar damage variable ranges from zero to unity (0: no damage, 1: crack opening). A crack extends progressively when the damage variable reaches the critical value of unity. The simulation in Fig. 27 was made assuming a very low hypothetical toughness (2MPa√m) and very low tensile fracture stress (500MPa) for the tungsten block

to reveal the most probable potential crack pattern for a conservative prediction. According to the recent neutron irradiation test study, the toughness and tensile strength of a commercial grade tungsten material (AT&M) reached roughly 10MPa√m (0.7 dpa, 500-600°C) and 1200MPa (1 dpa, 400-560°C), respectively [53]. Therefore, the predicted cracking behavior in Fig. 27 represents a very conservative prediction. Below 500°C, the irradiated tungsten (AT&M) exhibited perfect embrittlement (no plastic strain). Thus, a linear-elastic behavior was assumed for the tungsten block.

Fig. 27 shows that two cracks are formed in the cold ligaments of the tungsten block (<300°C) initiating from the interface to the interlayer already in the first heating cycle. Once initiated, the cracks are readily stabilized and do not grow anymore in the following load cycles. Fig. 27 reveals the prismatic form of the crack flanks. Although the relative size of the cracks is large compared to the ligament section (3×12mm²), the predicted crack pattern looks subcritical because the cracks do not interrupt the main heat conduction paths. The locations of crack formation match well with the regions of tensile stress concentration in the armor block. The actual stress in the stress hot spot will be relaxed upon cracking by releasing stored strain energy. As the heating imposes a strain-controlled load, the crack-tip stress intensity will be relaxed as the cracks grow beyond certain critical size. An open issue here is the potential risk of fatigue fracture. If there is no pre-existing crack (particularly in the ligaments), the incubation time to fatigue crack initiation will largely determine the life. A caveat is that the effect of singular stress concentration at the free surface edge of the interface needs to be clarified. Paris' law-type fatigue crack growth data are also needed.

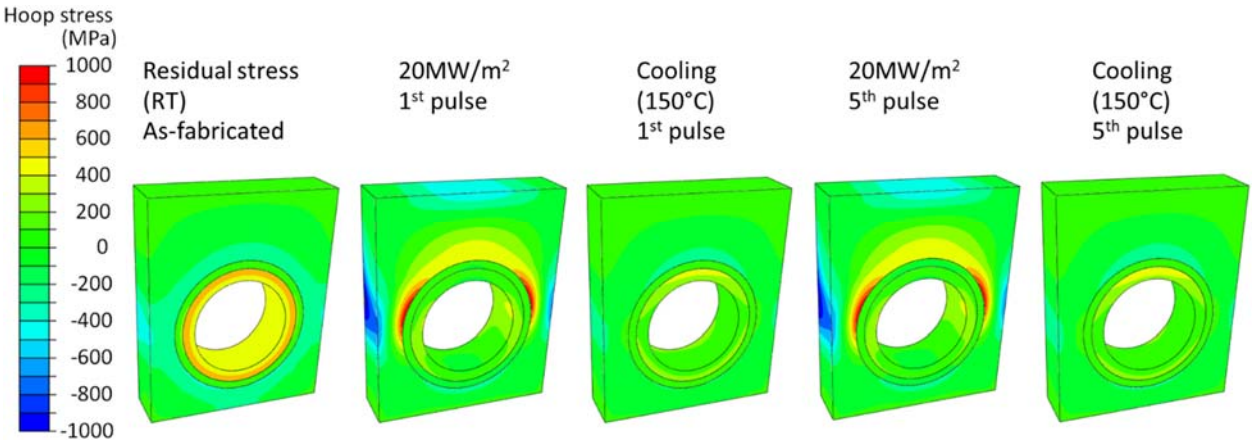

Fig. 26. Hoop stress states in a target monoblock unit after fabrication, under the HHF loading at 20MW/m² (1st and 5th cycle) and cooling phase at 150°C (1st and 5th cycle) (block dimension: 28×23×12mm³, armor thickness: 8mm). A very low hypothetical toughness (2MPa√m) and tensile stress (500MPa) was assumed for tungsten to take into account irradiation-induced degradation of material.

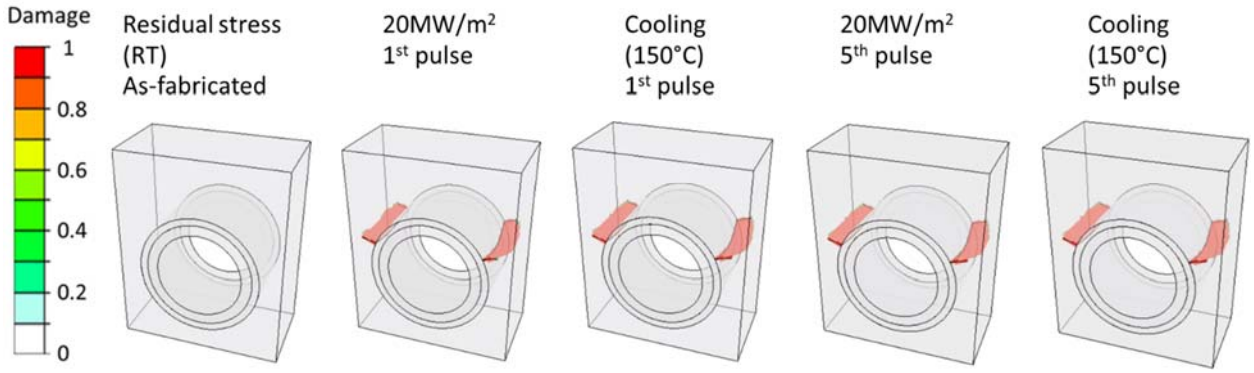

Fig. 27. Interior extension of the cracks formed in the fully irradiation-embrittled tungsten monoblock under the cyclic HHF loads of 20MW/m². For a conservative prediction, a very low hypothetical tensile fracture stress (500MPa) and fracture toughness (2MPa√m) was assumed to reveal the potential crack pattern.

7. Summary and conclusions

In this article, we discussed some modelling issues arising in the practice of the design-by-analysis approach for DEMO divertor target. Particularly, those issues were highlighted which may have a substantial impact on the assessment of structural integrity and lifetime. These issues were inherently related to the peculiar features of the component structure (multi-materials joint incl. soft constituent) and the nature of the applied loads (e.g. cyclic high heat flux, neutron irradiation) [54]. The uncertainty and limitations implicit in lifetime projection was examined by means of FEM simulation for diverse case studies. Distinct consequences of limited knowledge on the actual state of materials and effective loading history were discussed in the light of expected failure modes. Outstanding modelling issues needing further clarification were identified as summarized below in Table 2.

Table 2. Summary of the outstanding modelling issues identified for expected failure modes

Component	Issues	1) Description, 2) Consequences, 3) Impact on the assessment of structural integrity and lifetime
Cooling pipe (CuCrZr)	Initial residual stress	1) Stress evolution under cyclic HHF loads depends on the initial residual stress which is rarely known. 2) Substantial uncertainty in stress assessment. (medium risk) 3) Major impact
	Elastic shakedown	1) Stress state remains within the elastic regime. 2) No plastic strains, thus no risk of fatigue damage. (beneficial) 3) Major impact
	Stress-temperature phase offset	1) The stress/temperature pair varies either in an in-phase or off-phase mode depending on position and residual stress. 2) Location-dependent failure assessment. (medium risk) 3) Major impact
	Softening by thermal ageing	1) Initial yield strength can be lost due to long-term thermal ageing. 2) Plastic strain concentration near the free edge. (medium risk) 3) Major impact
	Coolant temperature, embrittlement	1) Toughness and total elongation of the irradiated alloy exhibit an opposite temperature-dependence to each other. 2) A narrow operational temperature range. (medium risk) 3) Minor impact
Interlayer (copper)	Strain concentration, fatigue life	1) If copper remains soft, substantial cyclic plasticity occurs with strain concentration near the free edge. 2) LCF limiting lifetime. (medium risk) 3) Major impact
	Ratchetting	1) If copper remains soft, progressive cyclic plastic deformation occurs leading to ratchetting to a certain extent. 2) Modest change in dimension and clearance (medium risk) 3) Minor impact
	Irradiation embrittlement	1) If helium production through transmutation in irradiated copper is significant, the interlayer becomes harder and brittle. 2) Higher tensile stress in the tungsten block. (modest risk) 3) Medium impact
Armor block (tungsten)	Impact of irradiation	1) Neutron irradiation of a low-quality tungsten may cause a strong reduction of strength and toughness. 2) Formation of subcritical cracks in the ligaments (modest risk). 3) Minor impact

Since these outstanding issues deal with the essential elements of structural integrity and the key items of lifetime assessment, the uncertainties need to be resolved, especially by closing the gaps in materials data, to enhance the credibility of the lifetime prediction based on the design-by-analysis approach.

References

[1] M. Turnyanskiy, et al., Fus. Eng. Des. 96-97 (2015) 361-364.
[2] R.A. Pitts et al., Nucl. Mater. Ener. 20 (2019) 100696.
[3] N. Asakura et al., Fus. Eng. Des. 136 (2018) 1214-1220.
[4] F. Maviglia, et al., Fus. Eng. Des. 109-111 (2016) 1067-1071.
[5] S. Noce, et al., Fus. Eng. Des. 155 (2020) 111730.
[6] M. Li, et al., Fus. Eng. Des. 90 (2015) 88-96.
[7] M. Li, et al., Fus. Eng. Des. 89 (2014) 2716-2725.
[8] M. Li, et al., Fus. Eng. Des. 101 (2015) 1-8.
[9] M. Li, et al., Nucl. Mater. Ener. 2 (2015) 1-11.
[10] M. Merola, et al., J. Nucl. Mater. 283-287 (2000) 1068-1072.
[11] G. Vieider, et al., Fus. Eng. Des. 46 (1999) 221-228.
[12] T. Hirai, et al., Phys. Scr. T159 (2014) 014006 (5pp).
[13] ITER structural design criteria for in-vessel components G 74 MA 8 01-05-28 W0.2.
[14] V. Barabash, et al., J. Nucl. Mater. 417 (2011) 904-907.
[15] W. Timmis, Material assessment on the use of copper alloys in DEMO, EFDA Report WP12-MAT02-M03, 2013.
[16] J.H. You, et al. Nucl. Mater. Ener. 16 (2018) 1-11.
[17] H. Greuner, et al., Fus. Eng. Des. 146 (2019) 216-219.
[18] H. Greuner, et al., Phys. Scri. T171 (2020) 014003 (7pp).
[19] J.H. You, et al., J. Nucl. Mater. (2020) in press.
[20] M. Gorley, et al., Fus. Eng. Des. 136 (2018) 298-303.
[21] M. Fursdon et al., Fus. Eng. Des. 146 B (2019) 1591-1595.
[22] M. Fursdon, et al., Fus. Eng. Des. 147 (2019) 111234.
[23] M. Fursdon, et al., Fus. Eng. Des. 160 (2020) 111831.
[24] J.H. You, et al., Nucl. Mater. Ener. 9 (2016) 171-176.
[25] J.H. You, et al., Fus. Eng. Des. 124 (2017) 364-370.
[26] G. Mazzone, et al., Fus. Eng. Des. 157 (2020) 111656.
[27] U. Bonavolontà, et al., Fus. Eng. Des. 159 (2020) 111784.
[28] M. Li, et al., Fus. Eng. Des. 102 (2016) 50-58.
[29] J.H. You, DEMO Divertor Sub-system Requirements Document, EFDA_D_2NZGNG, 2020.
[30] C. Bachmann, DEMO Plant Description Document, EFDA_D_2KVWQZ, 2020.
[31] P.A. Di Maio, et al., Fus. Eng. Des. 136 (2018) 1438-1443.
[32] P.A. Di Maio, et al., Fus. Eng. Des. 146 (2019) 1764-1768.
[33] P.A. Di Maio, et al., Fus. Eng. Des. 161 (2020) 111919.
[34] J.H. You, et al., Fus. Eng. Des. 109-111 (2016) 1598-1603.
[35] M. Li, et al., Fus. Eng. Des. 113 (2016) 162-170.
[36] M. Li, et al., Fus. Eng. Des. 124 (2017) 468-472.
[37] M. Li, et al., Nucl. Mater. Ener. 14 (2018) 1-7.
[38] S. Wurster, et al., J. Nucl. Mater. 442 (2013) S181-S189.
[39] J.H. You, Nucl. Fus. 55 (2015) 113026.
[40] S.A. Fabritsiev, et al., J. Nucl. Mater. 233-237 (1996) 513-518.
[41] J.H. You, Nucl. Mater. Ener. 5 (2015) 7-18.
[42] S. J. Zinkle, et al., Radiation and Thermomechanical Degradation Effects in Reactor Structural Alloys. in Structural Alloys for Nuclear Energy Applications. (2019) 163-210.
[43] G. Li, et al., Metall. Mater. Trans. A, 31A (2000) 2491.
[44] E. Melan, Ing. Arch. 8 (1938) 116-126.
[45] B.Y. Kim, et al., Fus. Eng. Des. 84 (2009) 1033-1037.

[46] J. H. You, et al., Fus. Eng. Des. 65 (2003) 483-492.
[47] S. Roccella, et al., Fus. Eng. Des. 160 (2020) 111886.
[48] G. Dose, et al., Fus. Eng. Des. 146 (2019) 870-873.
[49] S.A. Fabritsiev, et al., Plas. Dev. Oper. 5 (1997) 133-141.
[50] M. Richou, et al., Phys. Scr. T170 (2017) 014022 (7pp).
[51] M. Li, et al., Fus. Eng. Des. 122 (2017) 124-130.
[52] ABAQUS Analysis User's Guide, 2016, Dassault Systèmes.
[53] D. Terentyev, Private communication.
[54] M. Fursdon, et al., Fus. Eng. Des. 135 (2018) 154-164.

Acknowledgment

This work has been carried out within the framework of the EUROfusion Consortium and has received funding from the Euratom research and training program 2014-2018 and 2019-2020 under grant agreement No 633053. The views and opinions expressed herein do not necessarily reflect those of the European Commission. The authors are particularly grateful to Dr. Mike Fursdon (CCFE) for his highly qualified and inspiring discussions during the seven years of the WPDIV project period.

Data availability

The raw/processed data required to reproduce these findings cannot be shared at this time as the data also forms part of an ongoing study.